Ionics (2021) 27:4663–4672
https://doi.org/10.1007/s11581-021-04228-1

ORIGINAL PAPER

# Improved preparation efficiency and electrochemical performance of $LiNi_{0.8}Co_{0.15}Al_{0.05}O_2$ cathode material by oxalic acid and freeze-drying

**Zheng Song[1] · Xinfu Cao[2] · Can Cui[3] · Yang Zhang[1] · Jie Liu[1] · Fengsheng Li[1]**

Received: 5 May 2021 / Revised: 11 July 2021 / Accepted: 6 August 2021 / Published online: 25 August 2021


## Abstract

$LiNi_{0.8}Co_{0.15}Al_{0.05}O_2$ has attracted attention due to its high capacity and low cost. Herein, we report a method for the rapid and efficient preparation of NCA cathode materials using oxalic acid with freeze-drying techniques, and compare the differences of electrochemical properties for different metal concentrations. The solvent volatilization by liquid nitrogen freezing and freeze-drying techniques resulted in a more uniform mixing of metal ions while reducing the reaction time and energy consumption. The results characterized using X-ray diffraction revealed that the layered structure of the material was better and the cation mixing was lower when the metal ion concentration in the solution reached 0.15 mol $L^{-1}$. The electrochemical data revealed an initial charge–discharge capacity of 195 mAh $g^{-1}$ at 0.1 C, capacity retention of 88.75% for 100 cycles at 1 C, and a discharge capacity of 139.7 mAh $g^{-1}$ at 5 C. In addition, the cyclic voltammetry and electrochemical impedance spectroscopy reflect the material has low electrode polarization and excellent lithium-ion diffusion coefficient. The initial material diffusion coefficient is $2.673 \times 10^{-15}$ $cm^2S^{-1}$; after 50 and 100 cycles, it is $6.040 \times 10^{-16}$ $cm^2S^{-1}$ and $1.704 \times 10^{-16}$ $cm^2S^{-1}$ respectively. The results provide a new idea for the energy-efficient synthesis of $LiNi_{0.8}Co_{0.15}Al_{0.05}O_2$.

**Keywords** Cathode material · Co-precipitation · Lithium-ion batteries · $LiNi_{0.8}Co_{0.15}Al_{0.05}O_2$

## Introduction

With the rapid development of society and the increasing focus on environmental issues, this has led to a phenomenon: the rise of high-performance energy storage materials, which has shifted the focus from fossil energy to clean and renewable energy sources. In recent years, the popularity of electronic devices has further assisted in the development of energy storage materials [1–3].

The face of electronics has changed considerably since the first commercially available lithium-ion battery was introduced in 1991 [6]. $LiCoO_2$, as the most dominant commercial lithium battery, has long held a place in the field of energy storage. However, with the increasing awareness of environmental protection, $LiCoO_2$ with high Co content is gradually replaced by other materials [8, 13]. Later, $LiNiO_2$, $LiMnO_2$, and $LiFePO_4$ [9, 40] have got a couple of applications; problems such as low specific capacity, poor cycling performance, and poor thermal stability generally exist. Ternary cathode materials have been favored by researchers for their high energy density, excellent cycling performance, and thermal stability [5, 7]. Among Ni-rich based cathode materials, $LiNi_{0.8}Co_{0.15}Al_{0.05}O_2$, in which Ni and Co are co-located, is part of the most promising cathode materials due to its excellent electrochemical performance and structural stability [4, 10]. As a result, lithium-ion batteries have gradually evolved from inconspicuous 3C products to electric vehicles (EVs) [11], military equipment, and aerospace.

Contemporarily, the main methods for the preparation of cathode materials are as follows: high temperature solid phase [35, 36], co-precipitation [13, 17], spray pyrolysis method [14], hydrothermal method [15, 16], and sol–gel [25] synthesis. The co-precipitation method is the most

✉ Jie Liu
jie_liu_njust@126.com

[1] National Special Superfine Powder Engineering Research Center, Nanjing University of Science and Technology, Nanjing 210094, China

[2] Inner Mongolia Synthetic Chemical Engineering Institute, Huhhot 010010, China

[3] Bengbu Product Quality and Inspection Institute, Bengbu 233000, China

familiar method in NCA synthesis. Researchers have used CSTR [29] to flow at the same flow rate in different preparative solutions and to control experimental conditions such as reaction temperature, concentration, pH, and chelating agent [18]. Sith, the precursor and lithium sources are mixed by ball milling before calcination. This method has extraordinary facility requirements, a complex synthesis process and long residence time, raising costs to some extent. In a simple solid phase synthesis, it is difficult to form a homogeneous dispersion of the target product between each element.

Take into account these considerations, we need to find a more energy-efficient and simple method. In this paper, we present an improved co-precipitation method to prepare precursor materials. We will synthesize the precursor material at room temperature using oxalic acid as a precipitating agent and the lithium salt will be uniformly distributed in the solution by ultrasonic vibration in a wet process. As the lithium salts are dissolved in solution, it is not possible to obtain a uniformly mixed material by simple filtration, so the mixture is rapidly frozen in liquid nitrogen to remove the solvent by freeze-drying to obtain a hyperfine target product as a means of increasing the specific surface area and enhancing the diffusion of lithium ions. The whole reaction takes a short time, the metal ions are uniformly mixed, and the energy consumption is minimal.

## Experimental

### Sample preparation

Mainly, $Ni(CH_3COO)_2{\cdot}4H_2O$, $Co(CH_3COO)_2{\cdot}4H_2O$ and $AlCl_3{\cdot}4H_2O$ were dissolved in 100 mL of deionized water in the stoichiometric ratio of 0.800:0.150:0.050 to form an aqueous solution. Then, an appropriate amount of oxalic acid was added to the solution for 4 h reactions to obtain the precursor materials. Next, the solution was centrifuged 3 times with deionized water. After the final centrifugation, a suitable solution remained in the centrifuge tube, in which $LiOH{\cdot}H_2O$ with a metal-ion stoichiometry ratio of 1:1.05 was added, and the lithium salt was completely mixed into the solution by shock and ultrasound. Subsequently, the solution was rapidly frozen in liquid nitrogen and the solvent was evaporated by vacuum freeze-drying to obtain a fluffy and dry powder. The obtained dry precipitate was pretreated at 450 °C for 5 h and reacted at 750 °C for 12 h in a tube furnace with oxygen to obtain the product $LiNi_{0.8}Co_{0.15}Al_{0.05}O_2$. Under the oxygen atmosphere, $Ni^{2+}$ can be better converted to $Ni^{3+}$ to reduce the cation mixing emission. The preparation process is exhibited in Fig. 1. To compare the performance diversity under different metal-ion concentrations, altered concentrations of 0.05, 0.1, 0.15, and 0.2 mol $L^{-1}$ were prepared, naming them NCA-1, NCA-2, NCA-3, and NCA-4, respectively.

### Preparation of cathode electrodes and cell assembly

The cathode material, conductive super-P, and polyvinylidene difluoride were uniformly mixed in N-Methyl-2-pyrrolidone solution in the weight ratio of 8:1:1, and the slurry was made to reach sufficient viscosity by magnetic stirring. Then, the slurry was uniformly implemented onto the primed aluminum foil with a squeegee. The aluminum foil coated with slurry was made available for a vacuum oven and dried at 100 °C for 12 h.

The dried slurry was cut into 14-mm electrodes with a slicer, and then placed in an argon-filled glove box. Afterwards, the positive shell, positive plate, diaphragm, negative plate, and the negative plate were assembled together in sequence to make a button battery (CR2032). The electrolyte was 1 M $LiPF_6$ dissolved in EC/EMC/DMC (1:1:1 vol%).

### Material characterization

The crystal structure of the prepared materials was estimated by powder X-ray diffraction (XRD Bruker-AXS D8 Advance) in the 2 $\theta$ value range of 10°–80°, with a scan rate of 2° $min^{-1}$. Then, the morphological features and spatial distribution of the samples were observed by a field emission scanning electron microscopy (SEM FEI400FEG) equipped

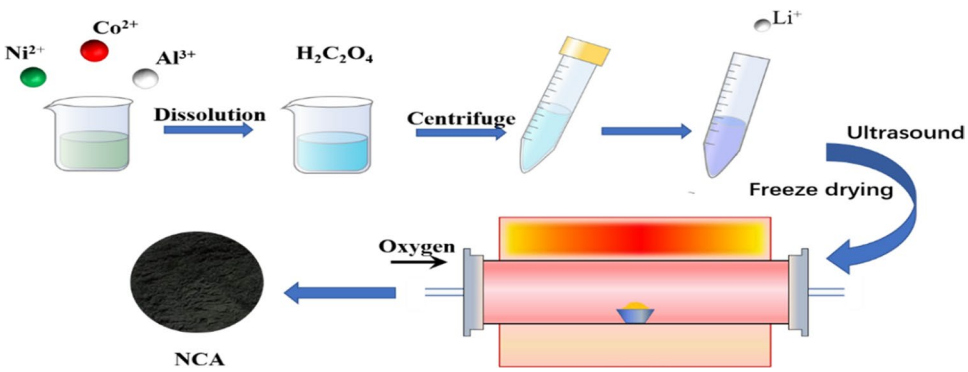


**Fig. 1** Preparation of $LiNi_{0.8}Co_{0.15}Al_{0.05}O_2$ cathode material

with an EDS energy dispersive X-ray spectrometer (Hitachi S-4800, Japan), and high-resolution transmission electron microscope (TEM JEM 2100F). The valence states of the sample surface elements were analyzed via X-ray photoelectron spectroscopy (XPS PHI QUANTERA), and the peak shape was fitted by XPS PeakFit.

### Electrochemical measurements

The charge–discharge tests were performed using the Land BT2001A automatic battery test system. The charge–discharge test was completed in the voltage range of 2.5–4.3 V and at different current densities. Cyclic voltammetry (CV) was carried out on a CHI660B electrochemical workstation (Chenhua, Shanghai, China) between 2.5 and 4.3 V at a scanning rate of 0.1 mV $s^{-1}$. The electrochemical impedance spectroscopy was measured by applying an AC voltage of 5 mV over a frequency range from 100 kHz to 10 mHz.

## Results and discussion

Figure 2 shows the XRD patterns of NCA materials at different concentrations ranging from 0.05 to 0.2 mol $L^{-1}$. It can be noted from Fig. 2(a) that all the samples conform to the layered structure of $\alpha$-$NaFeO_2$ [20] with R-3 m space group [12]. The characteristic peaks of each sample in the figure are quite sharp, showing brilliant crystallinity and pure phase. Figure 2(b–c) are enlarged images of $I$(006)/$I$(102) [19, 20] and $I$(018)/$I$(101). We can come to a conclusion that the peaks present a better splitting degree, indicating that the prepared NCA material has a lovely hexagonal crystal layered structure. The splitting degree of NCA-3 peak is the most pronounced, showing an excellent layered structure.

Table 1 displays the structure and cell parameters calculated based on XRD spectra. The presence of this $Ni^{2+}$ in NCA materials may occupy the position of $Li^+$ during the extraction/insertion of $Li^+$, resulting in $Li^+/Ni^{2+}$ blending and inducing irreversible capacity attenuation. We usually judge the degree of mixing by the ratio of $I$(003)/$I$(104) [21]. Studies show that when the ratio of $I$(003)/$I$(104) is greater than 1.2, which indicates a low degree of cation mixing; otherwise, it is the opposite. The lattice parameter $a$ reflects the slab space distance, and $c$ represents the interlayer spacing. When $c/a$ is greater than 4.9 [2], it displays the superior crystal morphology of the material, which is conducive to the formation of a more ordered hexagonal structure. From Table 1, it can be concluded that the ratios of $c/a$ and $I$(003)/$I$(104) for NCA-3 are 4.969 and 1.32, respectively, which are higher than those of other materials. It can be noticed that as the concentration of metal in solution increases, the lamellar structure of the material becomes more perfect and the degree of cation mixing decreases, reaching an optimum at 0.15 mol $L^{-1}$.

Figure 3(a–d) illustrates SEM photographs at different concentrations, energy spectrometer spectra, and high-resolution transmission electron microscopy of NCA-3. The NCA material has excellent morphology and crystallization, consisting of multiple rock-like shape particles with smooth

**Table 1** The structure characteristic of different samples

| Samples | $a$ (Å) | $c$ (Å) | $c/a$ | $V$ (Å$^3$) | $I$(003)/$I$(104) |
|---|---|---|---|---|---|
| S-1 | 2.876 | 14.224 | 4.946 | 101.87 | 1.19 |
| S-2 | 2.872 | 14.219 | 4.951 | 101.58 | 1.25 |
| S-3 | 2.871 | 14.268 | 4.969 | 101.88 | 1.32 |
| S-4 | 2.876 | 14.249 | 4.954 | 102.13 | 1.28 |

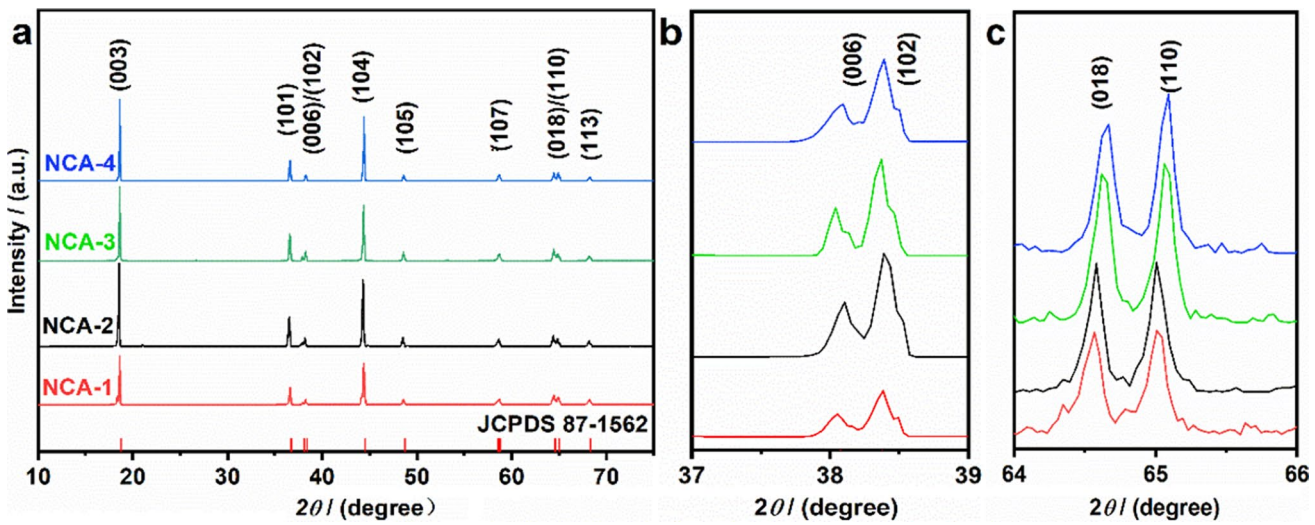


**Fig. 2** XRD patterns of samples under different reaction conditions

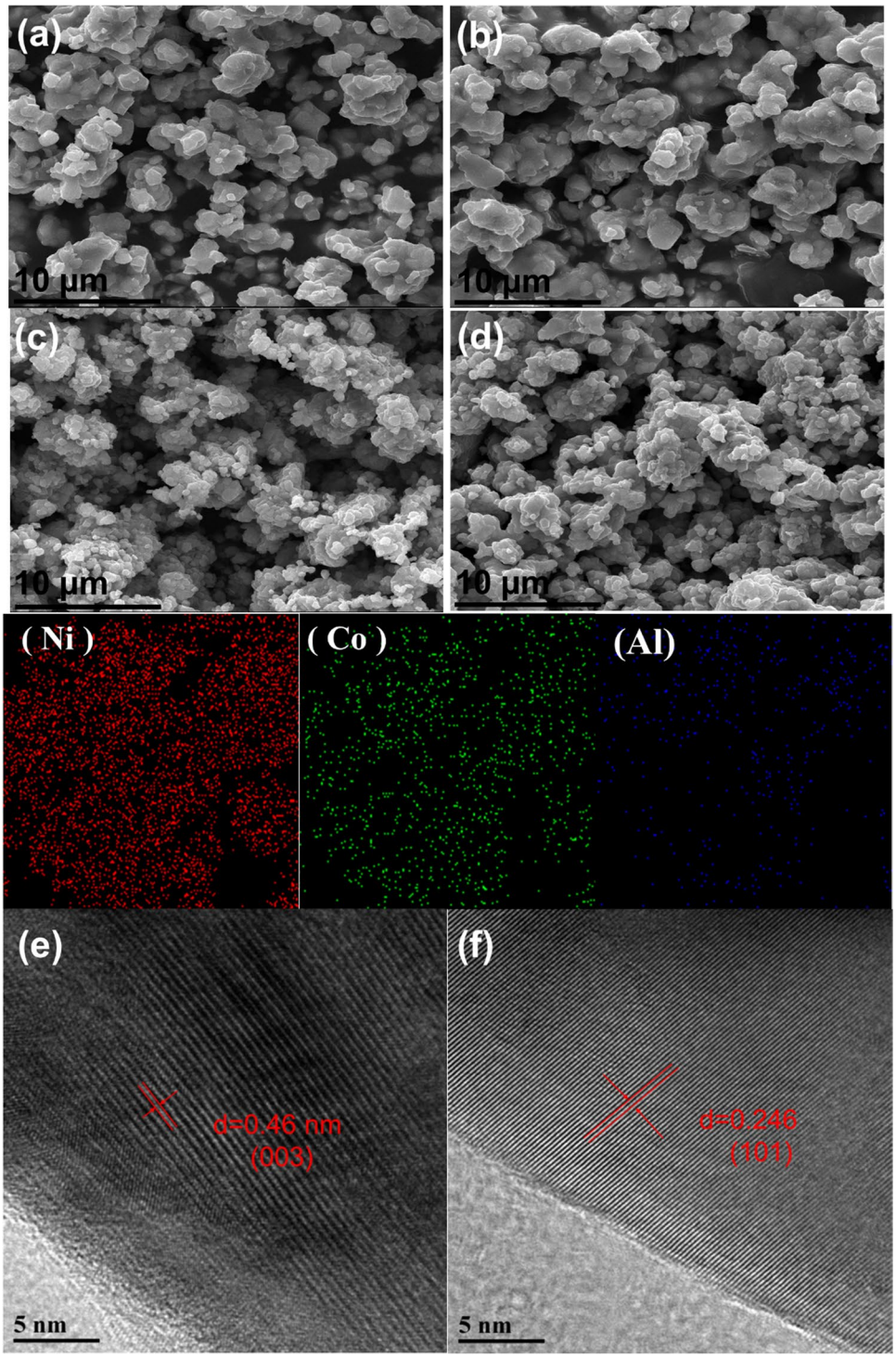


**Fig. 3** The SEM micrograph of NCA-1 (a), NCA-2 (b), NCA-3 (c), and NCA-4 (d); EDS mapping spectra of Ni, Co, Al element distribution on the surface of NCA-3 sample; HRTEM images of NCA-3 (e, f)

surface and tightly stacked with each other to pictures. As the concentration increases, the larger particles become composed of many smaller particles and the inter-particle agglomeration decreases, with a slight increase in agglomeration after 0.15 mol $L^{-1}$. The phase profile of NCA-3 has a large specific surface area, which facilitates the diffusion of $Li^+$ during charging and discharging. The distribution of Ni, Co, and Al in the material was examined to prove whether the internal element distribution of the NCA material prepared by oxalic acid was uniform. On the basis of EDS spectra, the elements Ni, Co, and Al are uniformly dispersed in the NCA cathode material that proved oxalic acid can be used to prepare NCA materials with homogeneous element distribution. As shown in the high-resolution TEM

(HRTEM) image (Fig. 3e–f) [37, 41], the sample shows good crystallinity with well-fined lattice fringes. The interplanar spacing is approximately 0.46 and 0.246, assigned to (003) and (101) planes of the layered R-3 m phase. In addition, the chemical composition of NCA-3 was determined using an inductively coupled plasma optical emission spectrometer (ICP-OES). The elemental amount of Ni, Co, and Al is 0.7919:0.1473:0.0470, which is consistent with the theoretical stoichiometry value.

For the purpose of exploring the influence of diverse concentrations on the structure of NCA cathode materials, XPS was used to detect the chemical valence states of materials [42, 43]. The main binding energy peaks of Ni, Co, Al, and O were detected in both NCA-4 and NCA-3 samples in Fig. 4(a–b). It can be clearly observed in Fig. 4(c–d) that the two main peaks of Ni $2p^{3/2}$ and Ni $2p^{1/2}$ of NCA-3 and NCA-4 are 855.4 eV and 872.9 eV [22], and their corresponding satellite peaks are 896.9 eV and 879.7 eV, respectively. XPSpeak software was utilized to fit the data. According to the spectrum of Ni $2p^{3/2}$ on the fitting curve at 854.7 eV and 856.7 eV, it could be divided into two peaks, $Ni^{2+}$ and $Ni^{3+}$, respectively. As seen in the figure, the $Ni^{3+}$ content of NCA-3 is 58.7%, which is higher than that of NCA-4, 52.9%. Apparently, the higher $Ni^{3+}$ content will reduce the $Ni^{2+}$-$Li^+$ mixing and exhibit better cycling performance [2], which is consistent with the previous XRD results. Figure 4(e–f) was the high-resolution spectrum of C 1 s, which respond well to hydrocarbon and carbonate, fitting the two binding energy peaks of 284.7 eV and 289.5 eV, respectively. This just goes to show that NCA-4 has more $Li_2CO_3$ phase than NCA-3 [18], which may be formed by residual lithium on the surface of the material with $H_2O$ and $CO_2$ in the air. Such carbonates formed will cause side reactions between the material and electrolyte, consuming extra $Li^+$ ions and causing irreversible loss of capacity. Figure 4(g–h) shows the high-resolution spectrum of O 1S [20], the peaks of lower binding energy at around 529.3 eV can be the lattice oxygen ($O_{lattice}$) derived from the crystal materials and the peaks of higher binding energy at around 531.3 eV can be assigned to the absorbed oxygen ($O_{absorbed}$) originated from the active oxygen species (LiOH and $Li_2CO_3$). We can conclude that the lattice oxygen of NCA-3 is 11.4% higher than that of NCA-4 (9.4%), indicating that NCA-3 has more metal-O bonds to stabilize the crystal structure of materials.

Figure 5 is the electrochemical test plots of the cathode materials. Figure 5(a) shows the initial charge–discharge curves of the material with different concentrations at 0.1 C. All specimens show typical stable charging voltages around 3.6 V, which is commensurate with the $Ni^{2+}$/$Ni^{4+}$ oxidation–reduction process [23]. The initial charge specific capacity drops from 195 mAh $g^{-1}$ to 180 mAh $g^{-1}$, which can be attributed to a fact: material structure is more suitable for the extraction/insertion of lithium ions at a concentration of 0.15 mol $L^{-1}$, so as to obtain a better capacity. Figure 5(b) shows the rate performance curves at different rates. The cells were all charged and discharged at rates of 0.1, 0.2, 0.5, 1, 2, 5, and 0.1 C for continued 5 cycles, respectively. A phenomenon was found where the discharge capacities of NCA-3 were 214.3, 203.0, 192.4, 178.3, 165.9, 139.7, and 205.5 mAh $g^{-1}$ at 0.1, 0.2, 0.5, 1, 2, 5, and 0.1 C, respectively, showing excellent electrochemical properties, probably due to the low doping of $Ni^{2+}$/$Li^+$ and low charge transfer resistance. Figure 5(c) shows the change in capacity of the cathode material after 3 activations at 0.1 C followed by 100 cycles at 1 C. We can find that the capacity retention rate of each sample is 69.10%, 73.29%, 88.75%, and 78.49%, which is consistent with the previously discussed structure and valence state of element. In other words, with an appropriate concentration of 0.15 mol $L^{-1}$, the as-prepared materials can present excellent cycle, which can be partly attributed to the decreasing $Li^+$/$Ni^{2+}$ mixing degree that can evidently enhance the integrality of the ordered hexagonal structure.

CV can help understand the electrochemical reactions during charge–discharge processes [44, 45]. To further investigate the deviations of NCA-3 and NCA-4 during charging and discharging, cyclic voltammetry was used to conduct the test at a scanning speed of 0.1 mV $s^{-1}$ under 2.5–4.3 V. Figure 6 illustrates the first three cycles of the CV curves of NCA-3 and NCA-4. Usually, the peaks in the CV curve correspond to the redox reactions during Li insertion and extraction, corresponding to the oxidation and reduction between $Ni^{2+}$ and $Ni^{4+}$. Due to the irreversible activation, the initial anode peak is very different from the one that follows. We usually use the potential difference between the redox peak to reflect the electrochemical reversibility of the cathode material. When the potential difference between the peak is small, it indicates that the material has excellent reversibility and low side reaction between the electrode and the electrolytic salt, vice versa [24, 25]. The initial oxidation and reduction peaks of NCA-4 are centered at 3.901 and 3.658 V, respectively, which are assigned to the extraction and insertion of Li ions. Clearly, the initial oxidation peak of NCA-3 is a little lower compared to NCA-4. The potential differences (0.171 V) for the redox peaks of NCA-3 are considerably smaller than that of NCA-4 (0.234 V), indicating better electro-chemical reversibility and lower interfacial polarization [39].

On behalf of analyzing the interfacial impedance and lithium-ion diffusion coefficient of the electrode under multiple cycles, electrochemical impedance spectroscopy was performed on the material, as shown in Fig. 7. The plots are the EIS atlas of the two materials cycled once, 50 times and 100 times, respectively. There is a semicircle in the mid-high frequency region and a straight line in the low frequency region. The semicircle corresponds mainly to the internal resistance

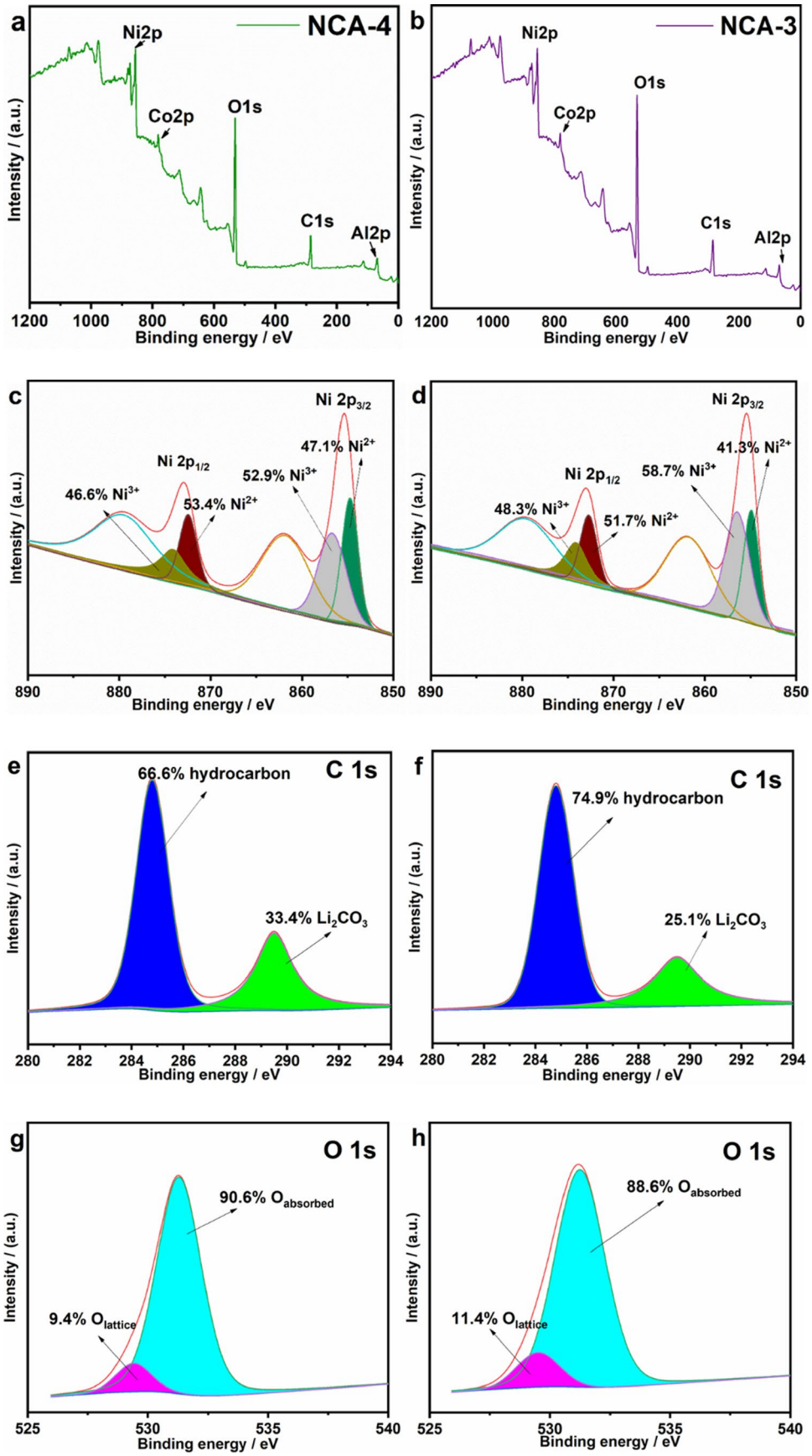


**Fig. 4** XPS spectra of NCA-4 (a) and NCA-3 (b), Ni 2p, O 1 s and C 1 s of NCA-4 (c, e and g), and NCA-3 (d, f, and h)

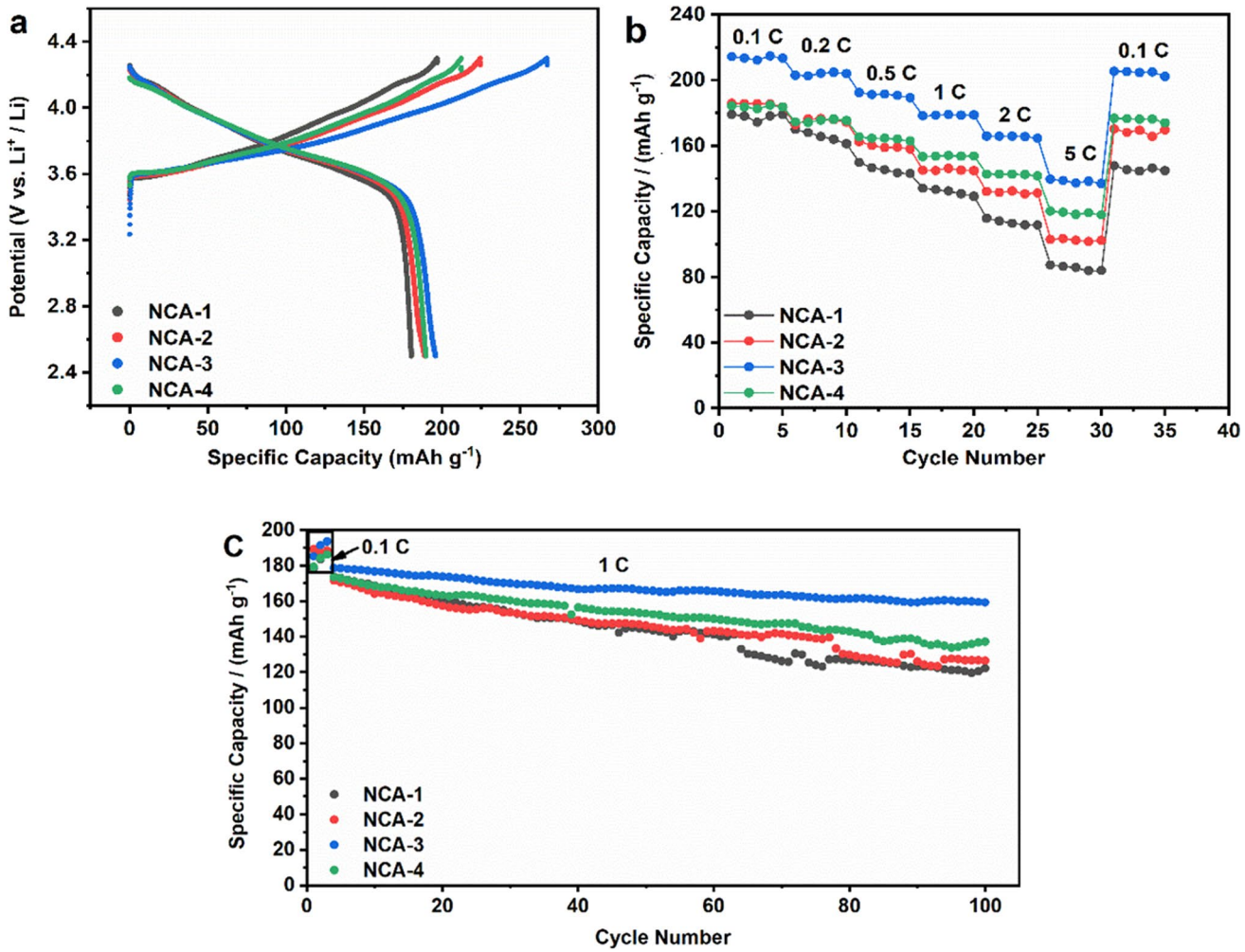


**Fig. 5** Initial charge/discharge curves at 0.1 C (a), rate capability (b), the cycling performance at 1 C (c)

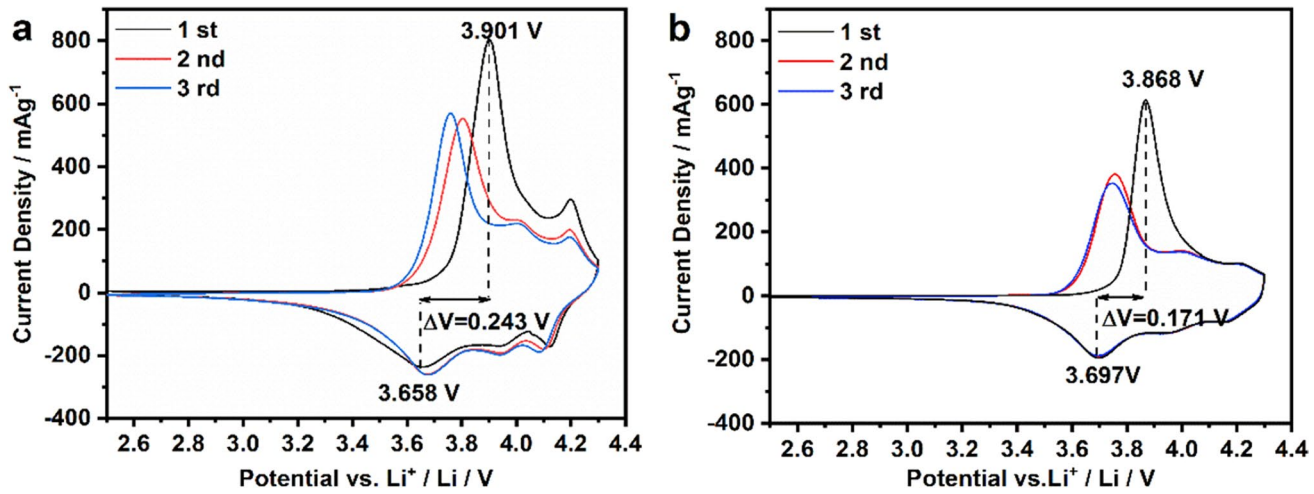


**Fig. 6** Cyclic voltammetry curves at scan rate of 0.1 mV $s^{-1}$ for the first three cycle of (a) NCA-4 and (b) NCA-3 cathode material at 2.5–4.3 V

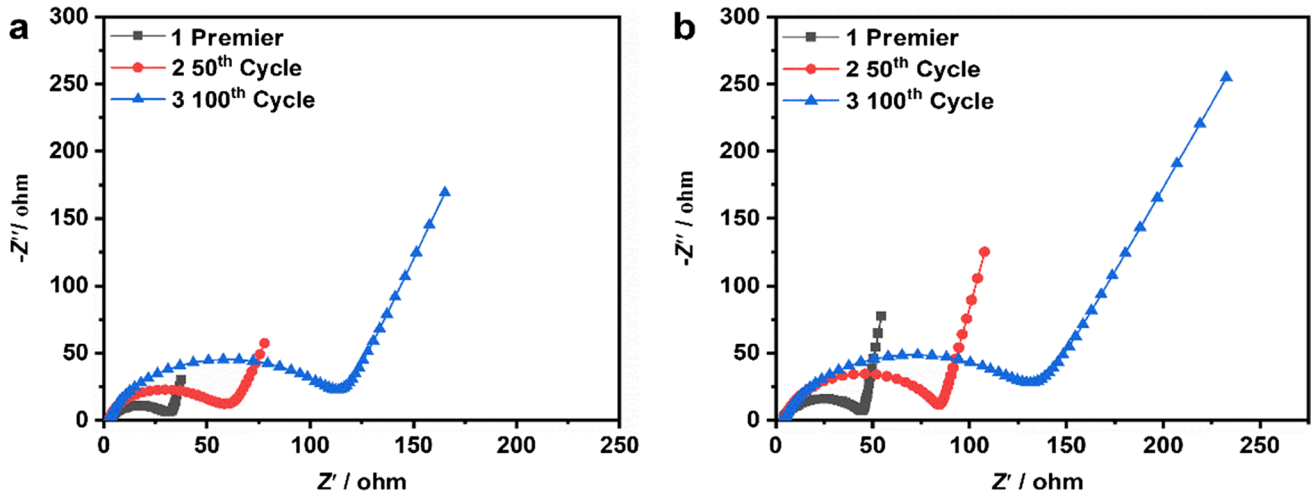


**Fig. 7** Nyquist plots of NCA-3 (a) and NCA-4 (b) after first, 50th, 100th cycle

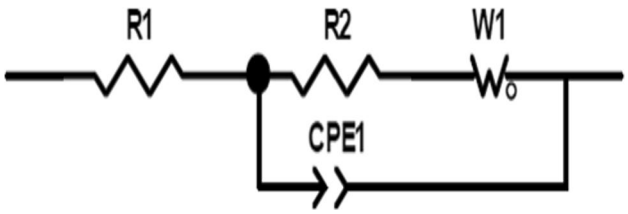


**Fig. 8** Equivalent circuit diagram

$R_s$ of the battery and the charge transfer resistance $R_{ct}$ of the battery electrolyte [26, 27, 38]. The line corresponds to the Warburg impedance during the diffusion of $Li^+$ in the cell. We established a simple equivalent circuit model of the software ZView, as shown in Fig. 8, and the specific parameters of the fitting are listed in Table 2. In light of relevant data, *CPE* is the analogous constant phase element and *W* is related to the solid-state diffusion of lithium ions in active materials corresponding to the straight line at low frequencies [28, 29]. For both samples, $R_s$ enhanced gradually after several cycles, manifesting the internal decomposition of the electrolyte and the increase of the internal resistance. Meanwhile, the charge transfer resistance $R_{ct}$ of the battery also increased behind manifold cycles, whereas the value of NCA-3 was always lower than that of NCA-4, proving that the internal structure of the electrode was stable, the side reactions between electrolyte and material were feeblish, and the cycling performance of the electrode was wonderful under this reaction condition [30].

The diffusion coefficient of lithium ion $D_{Li+}$ can be obtained by the following formula 1, where $R$ is the gas constant, $T$ is the absolute temperature, $A$ is the cathode surface area, and $n$ is the number of electrons per molecule during oxidation [31, 32]. $F$ is the Faraday constant, $C$ is the lithium ion concentration, and $\sigma$ is the Warburg factor. The Warburg factor is calculated by the following formula 2, $\omega$ is a low frequency, $Z_{re}$ is plotted from the data with $\omega^{-1/2}$, and the slope is the Weber factor $\sigma$, as shown in Fig. 9. The diffusion coefficient of lithium ion is calculated by substituting into formula 1, and the result is shown in Table 3. Analyzing the data reveals that the diffusion coefficient of $Li^+$ decreases after many loops, indicating that the extraction/insertion of $Li^+$ in the lattice is hindered and the internal resistance and polarization of the battery increase accordingly [24, 33]. However, the diffusion coefficient of NCA-3 is preferable to that of NCA-4. Combining cyclic voltammetry and comparison of charge–discharge properties, the cathode materials with better performance can be obtained under the experimental conditions of NCA-3.

$$D_{Li^+} = \frac{R^2T^2}{2A^2n^4F^4C^2\sigma^2} \quad (1)$$

**Table 2** Fitting results for electrochemical impedance spectra of two cells

| Samples | Premier | | 50th cycle | | 100th cycle | |
|---|---|---|---|---|---|---|
| | $R_s$(ohm) | $R_{ct}$(ohm) | $R_s$(ohm) | $R_{ct}$(ohm) | $R_s$(ohm) | $R_{ct}$(ohm) |
| A | 3.429 | 24.89 | 3.707 | 47.75 | 3.853 | 113.9 |
| B | 3.748 | 42.08 | 3.829 | 80.77 | 3.987 | 127.9 |

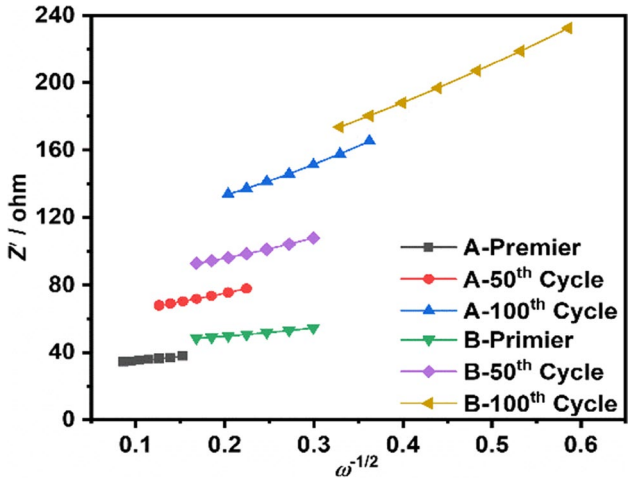


**Fig. 9** $Z_{re}$ as a function of square root of frequency ($\omega^{-1/2}$) for different numbers of cycles at the low frequency

**Table 3** Values of $D_0$ and $\sigma$ after different charge–discharge process

| | A | | B | |
|---|---|---|---|---|
| | $D_0$ ($cm^2S^{-1}$) | $\sigma(\Omega S^{-1})$ | $D_0$ ($cm^2S^{-1}$) | $\sigma(\Omega S^{-1})$ |
| Premier | $2.763\times10^{-15}$ | 46.561 | $2.818\times10^{-15}$ | 46.102 |
| 50th cycle | $6.040\times10^{-16}$ | 99.582 | $4.660\times10^{-16}$ | 113.357 |
| 100th cycle | $1.704\times10^{-16}$ | 187.467 | $1.138\times10^{-16}$ | 229.444 |

$$Z_{re} = R_s + R_{ct} + \sigma\omega^{-1/2} \quad (2)$$

$$\omega = 2\pi f \quad (3)$$

## Conclusion

In summary, $LiNi_{0.8}Co_{0.15}Al_{0.05}O_2$ ternary cathode material was successfully synthesized using oxalic acid and freeze-drying method. By comparing the electrochemical properties of the samples with different concentrations of metal ions, the results show that the NCA cathode material with higher capacity can be obtained when the metal ion concentration reaches 0.15 mol $L^{-1}$. It has a good layered structure, low cationic mixing, high rate capacity, and excellent cycling stability, which also proves its excellent electrochemical performance. Its initial discharge capacity at 0.1 C is 195 mAh $g^{-1}$, and the capacity retention at 1 C is 88.75% after 100 cycles. Furthermore, it exhibits excellent rate performance (139.7 mAh $g^{-1}$ at a rate of 5 C) due to the high lithium-ion diffusion coefficient. Cyclic voltammetry and electrochemical impedance spectroscopy also account for the material's lower battery polarization and better lithium-ion diffusion coefficient. This indicates that oxalic acid co-precipitation and freeze-drying method can successfully prepare ternary cathode materials, which can save reaction time, reduce energy consumption, and obtain more satisfactory electrochemical performance compared with the traditional co-precipitation method.

## CRediT authorship contribution statement

Zheng Song: investigation, writing—original draft. Xinfu Cao: visualization, investigation. Can Cui: software, validation. Yang Zhang: supervision. Jie liu: writing—review and editing. Fengsheng Li: writing—review and editing.

**Funding** This work was financially supported by the National Natural Science Foundation of China (NSFC,51606102) and the Priority Academic Program Development of Jiangsu Higher Education Institutions (PAPD).

## Declarations

**Competing interests** The authors declare no competing interests.

## References

1. Zhao X, Liu B, Yang J et al (2020) Synthesizing $LiNi_{0.5}Co_{0.2}Mn_{0.3}O_2$ with microsized peanut-like structure for enhanced electrochemical properties of lithium ion batteries. J Alloy Compd 832:154464
2. Nie Y, Xiao W, Miao C et al (2020) Effect of calcining oxygen pressure gradient on properties of $LiNi_{0.8}Co_{0.15}Al_{0.05}O_2$ cathode materials for lithium ion batteries. Electrochim Acta 334:135654
3. Nitta N, Wu F, Lee JT et al (2015) Li-ion battery materials: present and future. Mater Today 18:252–264
4. Zhang S-S (2020) Problems and their origins of Ni-rich layered oxide cathode materials. Energy Storage Mater 24:247–254
5. Sun H-H, Ryu H-H, Kim U-H et al (2020) Beyond doping and coating: prospective strategies for stable high-capacity layered Ni-rich cathodes. ACS Energy Lett 5:1136–1146
6. Chakraborty A, Kunnikuruvan S, Kumar S et al (2020) Layered cathode materials for lithium-ion batteries: review of computational studies on $LiNi_{1-x-y}Co_xMn_yO_2$ and $LiNi_{1-x-y}Co_xAl_yO_2$. Chem Mate 32:915–952
7. Ryu H-H, Park N-Y, Seo J-H et al (2020) A highly stabilized Ni-rich NCA cathode for high-energy lithium-ion batteries. Mater Today 36:73–82
8. Li W, Lee S, Manthiram A (2020) High-nickel NMA: a cobalt-free alternative to NMC and NCA cathodes for lithium-ion batteries. Adv Mater 32:2002718
9. Nie Y, Xiao W, Miao C et al (2020) Boosting the electrochemical performance of $LiNi_{0.8}Co_{0.15}Al_{0.05}O_2$ cathode materials in-situ modified with $Li_{1.3}Al_{0.3}Ti_{1.7}(PO_4)_3$ fast ion conductor for lithium-ion batteries. Electrochim Acta 353:136477
10. Xia S, Huang W, Shen X et al (2020) Rearrangement on surface structures by boride to enhanced cycle stability for $LiNi_{0.80}Co_{0.15}Al_{0.05}O_2$ cathode in lithium ion batteries. J Energy Chem 45:110–118

11. Hwang S, Chang W, Kim SM et al (2014) Investigation of changes in the surface structure of $Li_xNi_{0.8}Co_{0.15}Al_{0.05}O_2$ cathode materials induced by the initial charge. Chem Mater 26:1084–1092
12. Ito S, Fujiki S, Yamada T et al (2014) A rocking chair type all-solid-state lithium ion battery adopting $Li_2O$–$ZrO_2$ coated $LiNi_{0.8}Co_{0.15}Al_{0.05}O_2$ and a sulfide based electrolyte. J Power Sources 248:943–950
13. Dong H, Li S, Liu H et al (2019) Facile synthesis and electrochemical properties of $LiNi_{0.8}Co_{0.15}Al_{0.05}O_2$ with enlarged exposed active planes for Li-ion batteries. Ionics 25:827–834
14. Zhang J, Xu S, Hamad KI et al (2020) High retention rate NCA cathode powders from spray drying and flame assisted spray pyrolysis using glycerol as the solvent. Powder Technol 363:1–6
15. Zeng T, Zhang C (2020) Influence of the total metal ions concentration and CTAB on the electrochemical properties of NCA cathode synthesized by using urea precipitant. Ionics 26:127–139
16. Zhang Y, Cui C, He Y et al (2021) The effect of drying methods on the structure and performance of $LiNi_{0.5}Co_{0.2}Mn_{0.3}O_2$ cathode material for lithium-ion batteries. Mater Chem Phys 262:124269
17. Xie H, Du K, Hu G et al (2016) The role of sodium in $LiNi_{0.8}Co_{0.15}Al_{0.05}O_2$ cathode material and its electrochemical behaviors. J Phys Chem C 120:3235–3241
18. Hou P, Zhang H, Deng X et al (2017) Stabilizing the electrode/electrolyte interface of $LiNi_{0.8}Co_{0.15}Al_{0.05}O_2$ through tailoring aluminum distribution in microspheres as long-life, high-rate, and safe cathode for lithium-ion batteries. Acs Appl Mater Inter 9:29643–29653
19. Wang Y, Jiang J, Dahn JR (2007) The reactivity of delithiated $Li(Ni_{1/3}Co_{1/3}Mn_{1/3})O_2$, $Li(Ni0_{.8}Co_{0.15}Al_{0.05})O_2$ or $LiCoO_2$ with non-aqueous electrolyte. Electrochem Commun 9:2534–2540
20. Zhang Y, Qiu Z, Dong P et al (2018) One-step liquid-phase reaction to synthesize $LiNi_{0.8}Co_{0.15}Al_{0.05}O_2$ cathode material. J Mater Sci 53:13865–13874
21. Du Q-X, Tang Z-F, Ma X-H et al (2015) Improving the electrochemical properties of high-energy cathode material $LiNi_{0.5}Co_{0.2}Mn_{0.3}O_2$ by Zr doping and sintering in oxygen. Solid State Ionics 279:11–17
22. Huang Y, Huang Y, Hu X (2017) Enhanced electrochemical performance of $LiNi_{0.8}Co_{0.15}Al_{0.05}O_2$ by nanoscale surface modification with $Co_3O_4$. Electrochim Acta 231:294–299
23. Sun S, Liu T, Niu Q et al (2019) Improvement of superior cycle performance of $LiNi_{0.8}Co_{0.15}Al_{0.05}O_2$ cathode for lithium-ion batteries by multiple compound modifications. J Electroanal Chem 838:178–185
24. Zhu H, Li J, Chen Z et al (2014) Molten salt synthesis and electrochemical properties of $LiNi_{1/3}Co_{1/3}Mn_{1/3}O_2$ cathode materials. Synthetic Met 187:123–129
25. Han C-J, Yoon J-H, Cho W-I et al (2004) Electrochemical properties of $LiNi_{0.8}Co_{0.2-x}Al_xO_2$ prepared by a sol-gel method. J Power Sources 136:132–138
26. Lee D-J, Scrosati B, Sun Y-K (2011) $Ni_3(PO_4)_2$-coated $Li[Ni_{0.8}Co_{0.15}Al_{0.05}]O_2$ lithium battery electrode with improved cycling performance at 55°C. J Power Sources 196:7742–7746
27. Huang W-J, Zheng J-Y, Liu J-J et al (2020) Boosting rate performance of $LiNi_{0.8}Co_{0.15}Al_{0.05}O_2$ cathode by simply mixing lithium iron phosphate. J Alloy Compd 827:154296
28. Zhou J, Wang Q, Zhang M et al (2020) In situ formed $Li_5AlO_4$-coated $LiNi_{0.8}Co_{0.1}Mn_{0.1}O_2$ cathode material assisted by hydrocarbonate with improved electrochemical performance for lithium-ion batteries. Electrochim Acta 353:136541
29. Zhang N, Zhang X, Shi E et al (2018) In situ X-ray diffraction and thermal analysis of $LiNi_{0.8}Co_{0.15}Al_{0.05}O_2$ synthesized via co-precipitation method. J Energy Chem 27:1655–1660
30. Zhang X, Liu G, Li S et al (2019) Preparation of a homogeneous $Li_3PO_4$ coating and its effect on the electrochemical properties of $LiNi_{0.8}Co_{0.15}Al_{0.05}O_2$. J Electron Mater 48:4443–4451
31. Xia H, Liu C, Shen L et al (2020) Structure and thermal stability of $LiNi_{0.8}Co_{0.15}Al_{0.05}O_2$ after long cycling at high temperature. J Power Sources 450:227695
32. Liang M, Sun Y, Song D et al (2019) Superior electrochemical performance of quasi-concentration-gradient $LiNi_{0.8}Co_{0.15}Al_{0.05}O_2$ cathode material synthesized with multi-shell precursor and new aluminum source. Electrochim Acta 300:426–436
33. Cao C, Zhang J, Xie X et al (2019) A novel method for the modification of $LiNi_{0.8}Co_{0.15}Al_{0.05}O_2$ with high cycle stability and low pH. J Solid State Electr 23:1351–1358
34. Chen T, Li X, Wang H et al (2018) The effect of gradient boracic polyanion-doping on structure, morphology, and cycling performance of Ni-rich $LiNi_{0.8}Co_{0.15}Al_{0.05}O_2$ cathode material. J Power Sources 374:1–11
35. Xi Z, Wang Z, Peng W et al (2020) Effect of copper and iron substitution on the structures and electrochemical properties of $LiNi_{0.8}Co_{0.15}Al_{0.05}O_2$ cathode materials. Energy Sci Eng 8:1868–1879
36. Purwanto A, Yudha CS, Ikhwan Muhammad K et al (2020) Synthesis of $LiNi_{0.8}Co_{0.15}Al_{0.05}O_2$ cathode material via flame-assisted spray pyrolysis method. Adv Powder Technol 31:1674–1681
37. Liao K, Wei H, Shi P et al (2020) An exquisite electrode material using aramid nanofibers with enhanced discharge capacity and catalytic conversion of polysulfides. J Mater Chem A 8(40):21163–21172
38. Du J, Gao S, Shi P et al (2020) Three-dimensional carbonaceous for potassium ion batteries anode to boost rate and cycle life performance. J Power Sources 451:227727
39. Dai R, Zhang Y, Fan J et al (2020) Enhanced electrochemical kinetics and polysulfide traps of bifunctional perovskite promoter for highly stable lithium-sulfur batteries. ACS Sustain Chem Eng 8(50):18636–18645
40. He H, Chai Y, Zhang X et al (2021) A 2D–3D co-conduction effect in PEO-based all-solid-state batteries for long term cycle stability. J Mater Chem A 9(14):9214–9227
41. Zhang Y, Gu R, Zheng S et al (2019) Long-life Li–S batteries based on enabling the immobilization and catalytic conversion of polysulfides. J Mater Chem A 7(38):21747–21758
42. Zheng S, Zhang H, Fan J et al (2020) Improving electrochemical performance and safety of lithium-sulfur batteries by a "bullet-proof vest." ACS Appl Mater Inter 12(46):51904–51916
43. Huang Y, Cao S, Xie X et al (2020) Improving the structure and cycling stability of Ni-rich layered cathodes by dual modification of yttrium doping and surface coating. ACS Appl Mater Inter 12(17):19483–19494
44. Jamil S, Wang G, Yang L et al (2020) Suppressing H2–H3 phase transition in high Ni–low Co layered oxide cathode material by dual modification. J Mater Chem A 8(40):21306–21316
45. Jamil S, Ran Q, Yang L, et al (2021) Improved high-voltage performance of $LiNi_{0.87}Co_{0.1}Al_{0.03}O_2$ by $Li^+$-conductor coating. Chem Eng J 407:126442